*Advanced Materials Technologies*

ADVANCED MATERIALS TECHNOLOGIES
www.advmattechnol.com

RESEARCH ARTICLE OPEN ACCESS

# Optofluidic Raman Analysis and Capacity Recovery in Li-ion Cells

Ermanno Miele[1,2,3,4] | Wesley M. Dose[2,3,5,6] | Ian A. K. Davidson[7] | Hesham Sakr[7] | Natalie V. Wheeler[7] | Francesco Poletti[7] | Michael De Volder[3,6] | Clare P. Grey[2,3] | Jeremy J. Baumberg[1,3] | Tijmen G. Euser[1,3]

[1]Department of Physics, Nanophotonics Centre, Cavendish Laboratory, University of Cambridge, Cambridge, UK | [2]Yusuf Hamied Department of Chemistry, University of Cambridge, Cambridge, UK | [3]The Faraday Institution, Quad One, Harwell Science and Innovation Campus, Oxford, UK | [4]KnowLitech Ltd., Shaoxing, Zhejiang, China | [5]School of Chemistry, The University of Sydney, Sydney, New South Wales, Australia | [6]Department of Engineering, Institute for Manufacturing, University of Cambridge, Cambridge, UK | [7]Optoelectronics Research Centre, University of Southampton, Southampton, UK

**Correspondence:** Ermanno Miele (em730@cam.ac.uk) | Clare P. Grey (cpg27@cam.ac.uk) | Jeremy J. Baumberg (jjb12@cam.ac.uk) | Tijmen G. Euser (te287@cam.ac.uk)

**Received:** 22 October 2025 | **Revised:** 15 March 2026 | **Accepted:** 18 March 2026

**Keywords:** batteries | electrolyte | fiber sensing | operando | Raman

## ABSTRACT

Battery performance degradation arises from multifactorial and complex electrochemical processes involving all the battery components. Therefore, identifying and mitigating/suppressing the main degradation mechanisms is essential for deploying these technologies. Such a holistic understanding requires advanced and dedicated analytical tools as well as effective strategies to recover battery capacity, extend battery life, and facilitate second-life use and recycling of devices. Here, we develop a set of optical and microfluidic methodologies that enable *operando* chemical analysis of liquid electrolytes using Raman spectroscopy. We demonstrate that our methods have minimal perturbation on device operation and can be readily embedded in standard manufacturing processes. A bi-directional microfluidic access port allows the extraction and reinjection of carbonate-based electrolytes for analysis over hundreds of electrochemical cycles. Our data show that lithium salt anion ($PF_6^-$) degradation is a major source of electrolyte degradation and capacity loss in industrially relevant Li-ion pouch cells (Ni-rich layered cathodes (NMC811), and graphite anodes). The effects are particularly strong when cycled to an upper-cut voltage of 4.3 V. Finally, we demonstrate that battery capacity loss can be partially reversed by re-infusing pristine, uncycled electrolyte via an integrated microfluidic access port. This strategy not only mitigates degradation and extends battery life but also offers a practical pathway toward second-life applications and adaptable cell chemistries for future battery technologies.

## 1 | Introduction

Battery technologies are essential for achieving global sustainable energy goals, particularly in the context of transport and widespread automation. These developments will require an exponential growth in energy storage device production to enable widespread micro-mobility (transportation based on 2- and 3-wheel vehicles) in emerging markets, more efficient portable electronics, long-range unmanned (and manned) vehicles, and larger batteries for grid stabilization [1–7]. Li-ion batteries are still widely accepted as the battery technology of choice for most applications for the foreseeable future. The primary challenge in Li-ion technology is extending the device's lifetime while enhancing properties such as charging time and gravimetric and volumetric capacities [8–12]. Addressing these critical issues requires a multidisciplinary research approach. Furthermore, the

rapid expansion of Li-ion battery production has significantly increased the use of batteries in second-life applications [2, 6, 13, 14].

Li-ion batteries are complex devices, comprising a wide range of components that collectively contribute to their overall performance. Previously, research has mainly focused on optimizing device components independently, i.e., developing the positive and negative electrodes and their current collectors, the electrolyte with its salt, additives, and solvents, or the separators. For instance, there has been intense research on the positive electrode to understand the degradation mechanism of Ni-rich layered metal cathodes (NMC), develop alternative cathode materials, and improve their performance [13, 15–17]. It has recently become clear that complex electrochemical processes at the electrified surface of NMC cathode materials are a main cause of degradation [13–15, 18, 19]. For example, at high upper cut-off voltages (UCV > 4.2 V), degradation of Ni-rich positive electrode materials is exacerbated by lattice oxygen loss, surface reconstruction, and rock-salt phase formation, thereby limiting the practical voltage window these devices can operate in [20–23]. Electrolytes, especially those based on carbonate solvents, play a crucial role in the electrochemical degradation processes. The development of improved electrolyte chemistry [11–13, 15, 18, 24, 25] has therefore become a research priority. Electrolytes can be optimized by choosing of Li (or Na) salts and their concentration, solvent mixtures, and additives for specific cathode-electrolyte-anode combinations.

Overall, it is essential to emphasize that issues affecting a specific cell component also impact the functioning of the device's remaining components. For example, the electrochemical processes at the cathode can affect the electrolyte, producing degradation products that can diffuse through the cell and interact with processes occurring at the anode. Such effects are particularly strong in cell geometries with a lean electrolyte formulation (electrolyte-to-capacity-ratio < 20 μL $mAh^{-1}$) and components optimized for fast ion mobility. Examples of such unwanted interactions include SEI poisoning by transition-metal dissolution at NMC positive electrodes [26, 27] and subsequent modification of the ion solvation structure and solvation/desolvation processes at the cell interfaces [15, 28, 29].

Due to the electrolyte's involvement in a wide range of degradation reactions, its composition can provide an excellent indication of the battery's state of health. Electrolyte chemical composition monitoring thus enables the identification of by-products resulting from electrode material degradation. It helps provide a holistic understanding of device degradation processes, which is essential for preventing catastrophic failures and managing the device life cycle [2, 30–33]. It was recently shown that *operando* optical spectroscopy techniques, such as hollow-core-fibre-enhanced Raman [31] and fibre-based infrared absorption spectroscopy [30], enable non-destructive, molecular-level in situ analysis of electrolyte composition, offering direct insight into chemical changes associated with ageing and degradation processes [31].

In the meantime, the industry aims to deliver vehicle battery packs lasting up to 20 years [34]. To achieve this, strategies to mitigate degradation typically rely on improving charge/ discharge protocols, tuning the upper and lower cut voltages, and on-device maintenance/ packaging with effective thermal management [9]. While these approaches slow down degradation, only very few strategies have yet been proposed to "*actively*" rejuvenate or heal a degraded cell [10].

As a result, there has been limited progress in improving second-life readiness of Li-ion cells, with most strategies focusing on recycling rather than refurbishing devices. Likewise, no approaches have been demonstrated to future-proof Li-ion devices by making them upgradable with improved battery chemistries, such as new electrolytes as they become available [6, 13, 14, 18, 35].

Here, we demonstrate a non-invasive *operando* method for analyzing and, when needed, replenishing the electrolyte in a commercial Li-ion cell. Our results demonstrate that active electrolyte monitoring and controlled modification of the electrolyte volume throughout the device's life cycle can significantly extend device lifespan. In addition, the approach can be used to adjust the cell chemistry with minimal or no adverse effect on the device's performance.

## 2 | Results

This section outlines the development and implementation of a compact optofluidic platform for *operando* electrolyte sampling and analysis, establishing a framework for both diagnostic and restorative interventions in Li-ion battery systems.

### 2.1 | Optical and Microfluidic Access to Li-ion Batteries Electrolytes

Industrially relevant pouch cells (402035-size pouch cells) were modified to include a microfluidic access port (Figure 1a and Figure S1). After a desired number of charge/discharge cycles, a microsample (40-60 μL) of electrolyte is extracted using a standard pressure controller and flow meter (Figure 1b and Figure S2). The samples flow into a hollow-core optical fibre sensor whose excellent waveguiding properties enable enhanced chemical analysis by Raman spectroscopy (Figure 1c) [31]. Beyond sampling, the fluidic access port can also be used to replenish electrolyte, consumed by degradation processes over many cycles, with pristine uncycled electrolyte. We will show that such an "electrolyte transfusion" results in cell rejuvenation, including partial capacity recovery and device life extension.

The pouch cells comprise a nickel-rich NMC811 positive electrode and an artificial graphite negative electrode. The electrolyte was LP 57 (1.0 M $LiPF_6$ as lithium salt and a 3:7 Ethylene Carbonate (EC): Ethyl Methyl Carbonate (EMC) solvent mixture).

The experimental apparatus is composed of three setups. Microfluidic PEEK tubing is used to access the internal bottom compartment of the pouch cell (Figure 1a and Figure S1), which accommodates a standard electrolyte excess (the cell was loaded with 1.0 mL excess electrolyte). A microfluidics setup (Figure 1b) was constructed and actuated with $N_2$ using a pressure controller, with flow regulated by a flow meter. The setup enables the extraction of microsamples from the pouch cell electrolyte

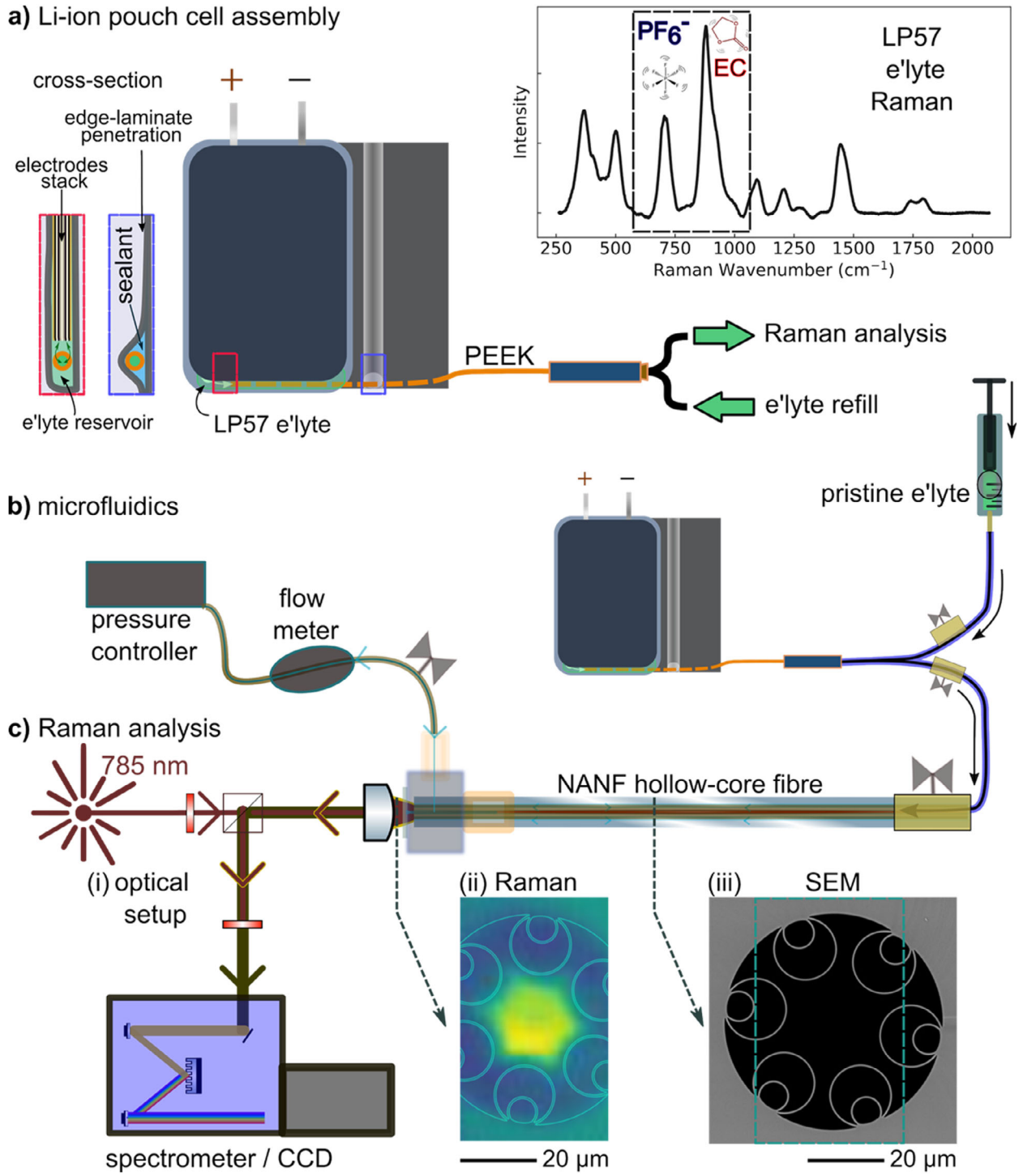


**FIGURE 1** | Optofluidic Raman analysis of battery liquid electrolytes and capacity recovery via electrolyte reinjection. a) High-energy NMC811/graphite pouch cells were provided with microfluidic access via edge-laminate penetration to enable LP57 (EC:EMC, 3:7 + 1 M $LiPF_6$) battery electrolyte (e'lyte) extraction using a pressure controller and flow meter. The schematic cross-sectional view highlights the electrode stack and excess electrolyte reservoir, indicating that the PEEK tubing is inserted through the laminate seal region without contacting the active layers, thereby preserving cell integrity. b) Pristine electrolyte refill was performed using the same microfluidic plugs. c) The extracted micro-sample is analyzed by Raman spectroscopy (i, ii) using as a sensing platform a Nested Antiresonant Nodeless hollow-core (NANF) fibre (iii shows SEM).

compartment and delivers them to the core of a Nested Antiresonant Nodeless Fibre (NANF) (Figure 1c-ii, 1c-iii and Figure S3), which serves as the Raman sensing platform [31, 32, 36]. A Raman pump laser (785 nm continuous wave, setup illustrated in Figure 1c-i) is launched into a NANF waveguide mode of the electrolyte-filled fibre core using an underfilled 10 × 0.3 NA microscope objective. Raman photons are scattered along the length of the fibre, part of them are captured in backward-propagating fibre modes that guide the light back to the proximate fibre facet. Our previous work [31] introduced a similar setup

that continuously monitored changes in electrolyte composition in a research pouch cell during its initial formation cycles. Here, we focus on monitoring the chemical composition of the electrolyte of a commercially relevant battery over a much longer timescale, as it degrades over many electrochemical cycles. For these new studies, the pouch cells are not continuously connected to the monitoring station; instead, they are connected for *on-demand* Raman analysis after a desired number of cycles. Typical microsample volumes are in the order of 40–60 µL, about 5% of the electrolyte contained in the cell. The sampled volume is larger than the internal volume of the NANF sensor (~40 nL/cm fibre length, 10–20 cm fibre length), which was preloaded with a small amount of pristine electrolyte to ensure fluidic continuity (details of the experimental procedure are provided in the Experimental Section and Figures S1, S3, S7, S8). Due to the small extracted volume, the micro-sampling method minimally perturbs the device's operation and has minimal effect on its performance.

## 2.2 | Electrolyte Extraction and Raman Collection over Multiple Cycles of Battery Operation

As a case study for our electrolyte chemical diagnosis approach, we designed experiments to understand the effect of the upper cut-off voltage (UCV) on electrolyte ageing during battery cycling. The rationale for this investigation is that high-energy NMC positive electrodes exhibit increased surface reactivity with an increase in nickel content. In the case of NMC881, this reactivity is particularly pronounced, limiting the practical voltage window to 4.2 V as an upper limit.

To better understand the effect of the UCV, pouch cells using polycrystalline (PC) NMC 811 as the cathode were assembled (see Figure S1) and cycled at C/3 rate, according to a nominal pouch cell capacity of 200 mAh (Figure 2a-ii: 4.0 V UCV yellow trace, 4.3 V UCV blue trace). The cells were tested at two different UCV of 4.0 V (Figure 2a-i, yellow trace) where little or no impact of the positive electrode surface reactivity is expected, and at a higher UCV of 4.3 V (Figure 2a-i, blue trace, and Figure S2) where the effect of positive electrode surface reactivity is expected to affect battery performance and electrolyte composition.

Raman analysis was performed on extracted microsamples, after ageing the devices for 79 and 200 cycles, for both 4.0 V and 4.3 V UCV PC NMC 811 cathode batteries (Figure 2b-i,2b-ii, respectively). These sampling points were intended to capture early-, mid-, and late-stage ageing behavior. The Raman spectral window was selected to be in the region between 650 and 1100 $cm^{-1}$, where the molecular vibrations of electrolyte solvents (EC and EMC) and the $PF_6^-$ anion can be detected. Particularly relevant in these spectral regions are the EC skeleton mode (729 $cm^{-1}$) and its Li-solvation at 732 $cm^{-1}$, the $PF_6$ stretch at 740 $cm^{-1}$, the EC breathing mode (893 $cm^{-1}$) and the Li-solvation (906 $cm^{-1}$). While the finer EC and EMC modes are partially convoluted at the resolution used, the $PF_6$ mode – the main target of the current investigation – remains sufficiently isolated to allow a direct interpretation of the data. The results show that the molecular vibration associated with the $PF_6^-$ anion (740 $cm^{-1}$) evolves as a function of both cycling and the upper cut-off voltage (UCV) of the battery. Details on Raman spectroscopy measurements and Raman modes assignments are provided in Figure S3–S7 and Table S1. Representative spectra were fitted using Lorentzian components to evaluate the evolution of peak positions and relative spectral contributions (Figure S6). Due to partial overlap between Li-solvation at 732 $cm^{-1}$, the $PF_6$ stretch at 740 $cm^{-1}$, the fitting was used to support qualitative trend analysis rather than absolute concentration quantification.

Specifically, after just 79 cycles, batteries cycled at 4.3 V UCV show a much stronger decrease in Raman intensity of the $PF_6$ mode (down to 24% of the initial intensity) compared to that for batteries cycled at 4.0 V UCV (~93% of the initial intensity) (Figure 2b-i). Along with the $PF_6$ band intensity reduction, concurrent changes in the $Li^+$-EC breathing mode at 906 $cm^{-1}$ and $Li^+$-EC skeleton mode at 729 and 732 $cm^{-1}$ indicate a modification of the counter-anion solvation structure of EC. Although the spectral changes are not strictly linear in intensity, the evolution of the $Li^+$–EC solvation bands evolve the same qualitative trend as the $PF_6^-$ feature, consistent with a progressive modification of the electrolyte solvation structure during cycling. Interestingly, despite the striking differences in $PF_6$ band intensity, both cells retain approximately 95% of their initial capacity after 79 cycles (Figure 2a-i).

Electrochemical cycling was continued, with a second electrolyte micro-sample extraction and analysis scheduled at cycle 400. After 400 cycles, the capacity retention of the 4.3 V UCV cell had reduced to 50%, while the 4.0 V UCV cell still displays a capacity retention of 90% (Figure 2a-ii). This confirms that the choice of UCV is critical for battery ageing for this class of cathode materials. These results also indicate that the measured $PF_6$ Raman mode is predictive of battery capacity fade at much higher cycle numbers.

After 400 cycles, an electrolyte sample was extracted from the 4.0 V UCV cell and analyzed with Raman spectroscopy. Extraction of electrolyte after 400 cycles was found to be impossible due to an absence of flow from the cell to the hollow-core fibre for the 4.3 V UCV battery (blue line), suggesting significant electrolyte consumption/degradation for this higher UCV cycling regime. Figure 2 b-ii compares the Raman data between cycle 79 and cycle 400 extracted micro samples for the 4.0 V UCV cell and reveals a further 25% intensity drop of the $PF_6$ anion peak at ~740 $cm^{-1}$, suggesting that, at this lower UCV, capacity fade is also associated with a $PF_6$ anion degradation pathway, albeit at a much lower rate.

## 2.3 | Single-crystal NMC 811 Cathode Cells

To investigate whether the cathode material morphology affects its surface reactivity with the electrolyte, further experiments were carried out on full cells, now using single-crystal (SC) NMC811 cathodes. The batteries were assembled and aged in the same way as the polycrystalline NMC811 cell illustrated above. A UCV of 4.3 V was chosen as it provides a more stressful condition. As shown in previous reports, the cyclability of NMC811 cathode cells is greatly improved by the single-crystal morphology of the material [37–39]. An approximate 10% capacity fade is observed in the first 79 cycles (Figure 3a), with a capacity retention close to 90%. However, we also observed fluctuations of 5–10% in capac-

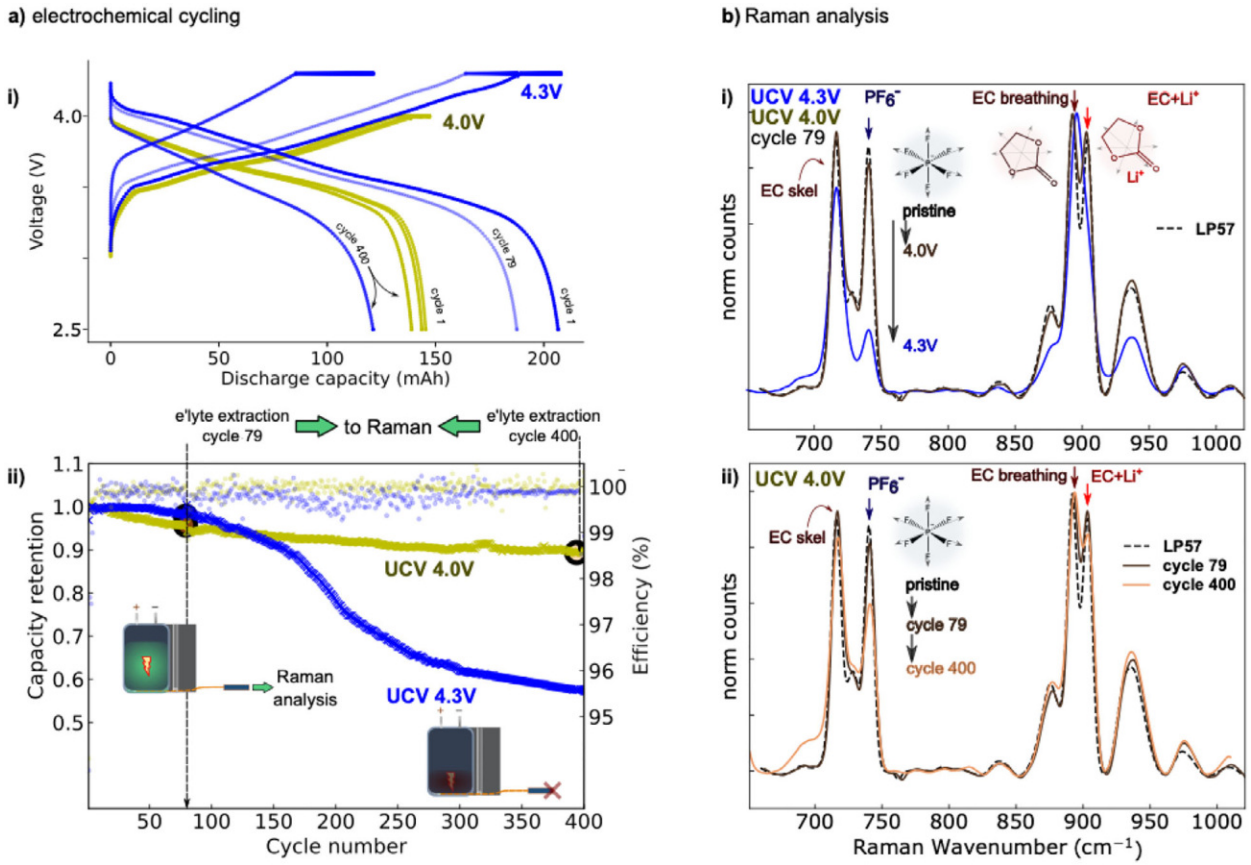


**FIGURE 2** | Battery cycling and electrolyte Raman analysis at the designed cycle point. a, Ageing cycles for 4.0 and 4.3 V at C/3 rate PC-NMC Li-ion pouch cells, with voltage vs. capacity shown above and capacity retention and Coulombic efficiency vs. cycle number shown below. (a) with electrolyte extraction at cycles 79 and 400 for Raman analysis. (b) i. Comparison of the Raman spectra of the pristine (uncycled) electrolyte (dashed lines) vs. cycle 79 of batteries cycled with 4.0 V and 4.3 V UCVs. ii. Comparison of the Raman spectra after no, 79, and 400 cycles using a 4.0 V UCV.

ity and coulombic efficiency during the first 79 cycles, which are likely caused by slight variations in the externally applied pressure on the pouch cell during this particular measurement. Despite this non-ideal cycling condition, the charge/discharge profile of the cells was not affected, as evidenced by the capacity vs. Voltage traces shown in the inset of Figure 3a. At cycle 79, Raman analysis was performed on an extracted micro sample of electrolyte using the hollow-core fibre setup (Figure 3b). The sample was reinserted into the cell after the measurement. After a further 131 cycles (at cycle 210, capacity retention equal to 88%), a second sample extraction and Raman analysis were performed.

In these SC NMC811 cells, the $PF_6^-$ anion band intensity is significantly reduced by approximately 55% after only 79 cycles. Interestingly, however, little further changes in Raman band intensity are observed in the subsequent 131 cycles (Figure 3b). Despite the significant drop in $PF_6$ Raman band intensity, the cell capacity (Figure 3a) stayed within ~90% of the initial value, even after 210 cycles. The Raman spectra also show significant changes in the solvation structure of $Li^+$-EC modes at 732 and 906 $cm^{-1}$, which are much stronger than those observed for the polycrystalline cells. Interestingly, at cycle 210, the EC Raman modes (at 729 and 893 $cm^{-1}$) also show increased intensity compared to the pristine and cycle 79 electrolyte samples. Because spectra were normalized to the total spectral area, this apparent increase likely reflects a redistribution of spectral contributions associated with electrolyte degradation rather than a direct increase in EC concentration, consistent with a reorganization of the $Li^+$ solvation environment during cycling.

## 2.4 | Electrolyte Refill via Microfluidic Reinjection and Capacity Recovery

These Raman experiments identified the consumption of $PF_6^-$ anions as a signature of significant capacity fade in polycrystalline cells. Therefore, to explore whether the lost capacity can be recovered, the cell's microfluidic access port was used to "transfuse" the cycled cells with pristine electrolyte. The polycrystalline NMC 811 cells were disconnected and moved into a dry room, where pristine electrolyte was added in a volume proportional to the lost capacity. Thus, ~200 µL of fresh LP57 electrolyte was added to the 4.0 V UCV cell and ~600 µL of LP57 to the 4.3 V UCV cell (details in Experimental section). After performing the electrolyte "top-up", the cells were left to rest for 4 days to allow for diffusion processes to mix the cycled and uncycled electrolytes. The cells were subsequently cycled using the same C/3 C-rate charge-discharge protocol for a further 200 cycles (Figure 4). The effect of the electrolyte reinjection was evaluated by fitting the capacity profile of the device with an exponential decay to extract the device's half-life (see Equations S1–S3).

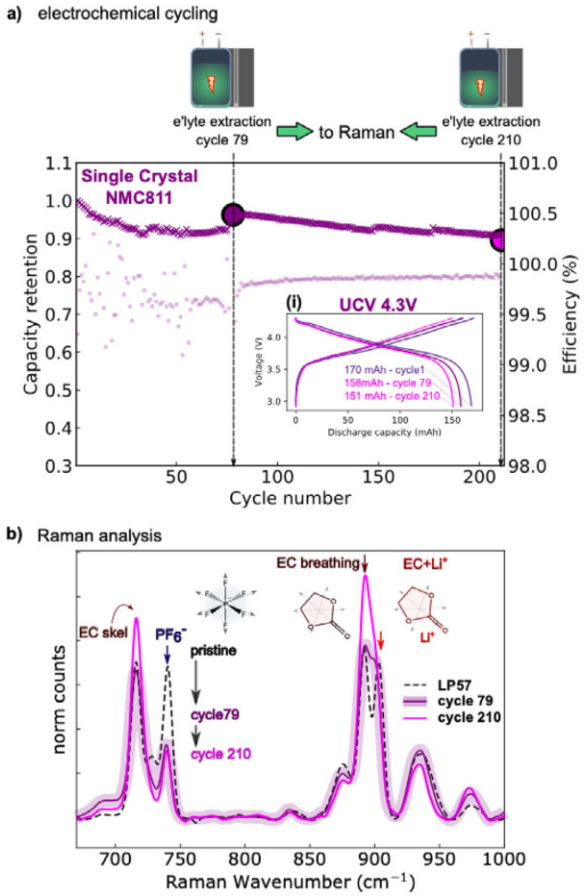


**FIGURE 3** | Multiple cycles Raman analysis of battery liquid electrolyte cycled in a single crystal NMC811 cell. a) Plot of (normalized) capacity retention (crosses) and Coulombic efficiency (open circles) vs. cycle number, showing where the samples were extracted for Raman analysis. We note that during the first 70 cycles, an imperfect stack pressure was applied to the pouch cell, which was corrected after cycle 70. The inset (i) shows the voltage vs. capacity curves for the first, 79th, and 210th cycles. b) Evolution of the Raman spectrum of LP57 electrolyte at cycle 79 (dark purple line, shaded region indicates the minimum and maximum between duplicates) and 210 (pink) of a single crystal NMC811 cathode Li-ion cell. Pristine LP57 electrolyte is displayed as a black dashed line. Relevant peaks are assigned.

Rather impressively, both the devices' half-lives and capacities significantly benefited from this straightforward, pristine electrolyte injection. For the 4.0 V UCV cell, we measured a capacity recovery of 7%; almost completely restoring the 10% capacity loss observed in the first 400 cycles. The half-life of the 4.0 V UCV cell was extended from 2700 cycles to ~4000 cycles. The cell cycled at the higher UCV of 4.3 V showed a 15% recovery, regaining one-third of the 45% capacity loss observed in the first 400 cycles. The 4.3 V UCV cell also demonstrated a fourfold increase in the projected device half-life, extending it from 500 to 2000 cycles. The higher predicted half-lives after electrolyte injection are ascribed to two phenomena: first, the electrolyte is added to a formed cell, the first formation cycle(s) consuming the most electrolyte salts to form both inorganic and organic SEI salts; second, the addition of more electrolyte increases the electrolyte flooding of the cell. The procedure was repeated on two single-crystal NMC cells cycled at 4.3 V UCV and found to also extend the device life for these devices by at least 200 more cycles (Figure S8).

## 3 | Discussion

We have demonstrated how commercial and industrially relevant pouch cells can be actively monitored during their lifetime to retrieve direct chemical information on the electrolyte composition.

Our Raman data confirm that part of the capacity fade is linked to modifications in the chemical composition of the electrolyte, particularly in the Raman mode of the $PF_6^-$ anion. This suggests that there are two primary reasons for battery capacity fade. The first one, commencing during the first formation cycle, is SEI formation at the graphite electrode. The second one, which is strongly affected by UCV, is cathode material degradation principally associated with previously reported electrochemical (side) processes at the cathode side, resulting in negative electrode slippage, electrolyte degradation, and SEI poisoning [15, 22, 27, 28, 40].

The third one, intertwined with the cathode degradation, is electrolyte consumption. Especially in lean electrolyte formulations, the reduction of viable anions and electrolyte solvents leads to a progressive capacity reduction and eventually to a sudden device failure after reaching a knee point, as seen in the polycrystalline 4.3 V UCV cell. The cycling behavior of the 4.0 V UCV cell indicates that when electrochemical cycling does not severely damage the cathode material, a major source of capacity fade is electrolyte consumption.

Strikingly, when the electrolyte pool is replenished by reinjection, the battery's capacity recovers significantly. Our data also reveal how single-crystal NMC materials are more resilient to ageing and appear to consume the electrolyte more slowly. This is even though we measure a loss of $PF_6^-$ similarly to polycrystalline NMC cycled at the same UCV, in comparison to that in the pristine electrolyte injection.

This apparent discrepancy between similar $PF_6^-$ degradation and improved capacity retention in single-crystal NMC cells suggests that electrolyte salt decomposition is not necessarily directly correlated with immediate electrochemical performance decay. Ni-rich layered oxides are known to catalyze electrolyte oxidation and dehydrogenation reactions at the cathode–electrolyte interface, generating protons and water that promote $PF_6^-$ decomposition into $PF_5$ and HF species. Such reactions may occur at comparable rates in both single-crystal and polycrystalline materials under similar high-voltage conditions. However, capacity retention is primarily governed by lithium inventory loss at the negative electrode, which arises from secondary reactions involving SEI evolution and electrolyte decomposition products. Polycrystalline cathodes may accelerate these secondary degradation pathways through increased surface area, grain-boundary reactivity, and microcrack formation, thereby promoting parasitic reactions that ultimately lead to faster capacity fade even when similar levels of $PF_6^-$ degradation are observed. These mechanisms are consistent with recent studies highlighting the catalytic

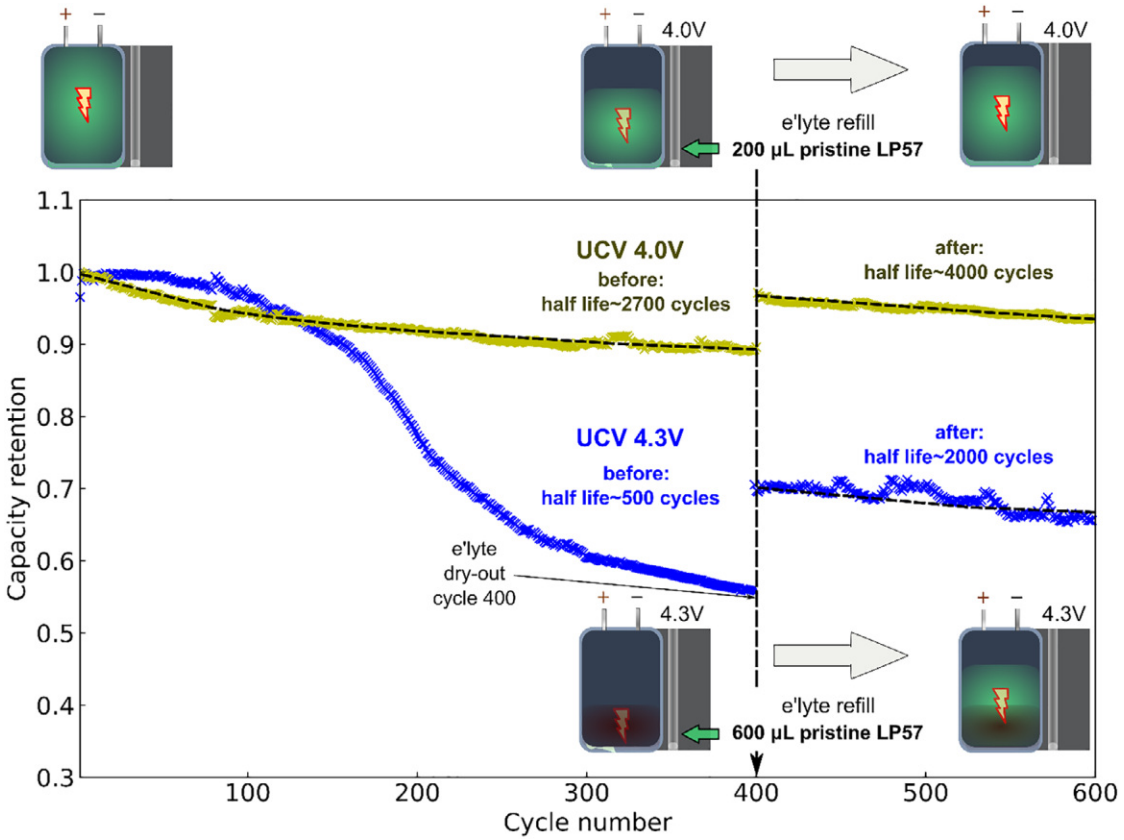


**FIGURE 4** | Battery refill with pristine electrolyte reinjection. Capacity retention vs cycle number, illustrating where cycled cells were rejuvenated by re-injecting pristine LP57 electrolyte using the microfluidic plugs previously used for electrolyte extraction after 400 cycles. Both cells recovered > 50% of the capacity lost in their first 400 cycles. For the 4.0 V (yellow trace) cell and the 4.3 V cell (blue trace), the capacity loss and half-life have been predicted by fitting the data with an exponential decay (See Equations S1–S3).

activity of Ni-rich cathodes and the complex coupling between electrolyte decomposition, lattice oxygen activity, and interfacial degradation processes [41–45].

Apart from healing degraded cells, the injection method could also be used to modulate the electrochemistry inside a Li-ion battery device during its lifetime. For instance, it is well known in the literature that, while cyclic carbonates are essential solvents (i.e., EC and VC) for SEI formation at the anode, they also pose challenges at the cathode-electrolyte interface, leading to significant electrolyte oxidation and salt hydrolysis [15, 41, 42, 46]. Built-in fluidic access ports may enable the use of different electrolytes for cell formation, cell cycling, and healing, with both electrolytes and additives optimized for each process. Notably, compositional changes in the electrolyte, such as salt depletion, may precede measurable capacity decay, with non-linear capacity fades [47, 48] highlighting the importance of correlating chemical evolution with complementary electrochemical diagnostics.

Ni-rich layered materials exhibit high reactivity with carbonate-based electrolytes, leading to dehydrogenation and oxidation pathways, as we have previously shown [31].

Here, thanks to the improved spectral resolution and the ability to decouple the sensing process from electrochemical cycling (since transition-metal dissolution and salt hydrolysis may take several cycles to manifest), we can specifically focus on the degradation pathways of these electrolytes. The specific reaction pathways related to the above processes include: EC oxidation to VC, which has previously been observed by *operando* Raman [31] and FT-IR [41] spectroscopy:

$$(CH_2O)_2CO \rightarrow (CHO)_2CO + 2e^- + 2H^+$$

Salt degradation, the focus of the current Manuscript, on the other hand, can be described as:

$$H^+ + PF_6^- \rightarrow HF + PF_5$$

More generally, an electrolyte solvent can undergo an oxidation reaction on the surface of NMC:

$$Li_xM_yO_z + LiPF_6 + El \rightarrow Li_x + 1M_yO_z + PF_{6-} + El^+$$

$$El^+ \rightarrow El^* + H^+$$

$$H^+ + PF_6^- \rightarrow HF + PF_5$$

where El is the electrolyte solvent, $El^+$ its oxidized species, El* its de-hydrogenated species. In these equations, it is assumed that

the cell is at OCV, hence the electrons and Li ions stay in the NMC. Finally, an oxygen loss reaction involving the electrolyte could take place, such as

$$(CH_2O)_2CO + 4O^* \rightarrow 2CO_2 + CO + 2H_2O + 4O_2 + \text{vacancy} + 8e^-$$

with the produced water, then reacting with the salt.

## 4 | Conclusions

Raman spectroscopy, utilizing hollow-core fibre sensors and a novel microfluidic access port to Li-ion cells, can be used to analyse commercial Li-ion pouch cells featuring a Ni-rich NMC cathode, graphite anode, and carbonated electrolyte. Using Raman spectroscopy, the decomposition of $PF_6$ anions and electrolyte volume consumption are identified as the primary degradation effects in high UCV cycling regimes. Measurements on single-crystal NMC 811 cathode cells demonstrate how the same UCV results in similar anion decomposition, as evidenced by the reduction in intensity of the corresponding Raman mode. Cells based on single-crystal NMC cathodes were more resilient to electrochemical cycling despite similar anion decomposition pathways.

The microfluidic access ports can also be used to reinject uncycled, pristine electrolyte into cycled cells. This simple procedure results in significant recovery of battery capacity and appears to significantly extend the lifetime of the cells.

Our microsampling approach paves the way to *operando* electrolyte battery monitoring using direct chemical analysis techniques, such as vibrational spectroscopy or chromatography methods. Our electrolyte infusion approach also opens up the prospect of modulating battery electrolyte chemistry during the device's lifetime. For instance, we can envision strategies for electrolyte exchange after cell formation by substituting the electrolyte with one tailored for prolonged cycling or dedicated fast-charging applications. The methods introduced here also future-proof Li-ion battery technology by enabling devices to be upgraded with next-generation electrolyte formulations, significantly enhancing their second-life applications.

## 5 | Methods

### 5.1 | Pouch Cell Preparation and Microfluidic Port Assembly

Pouch cells were received dried and sealed from LiFun (China). We used both Polycrystalline and Single Crystal NMC811 positive electrode cells. The negative electrode was Natural graphite, as stated by the manufacturer. Cells were stored in a glovebox ($H_20 < 0.1$ ppm and $O_2 < 0.1$ ppm) before opening. After opening the cell, it was dried under dynamic vacuum at 110°C for at least 2 h, followed by 5 cycles of Ar purge/pump. All the microfluidic parts (tubing, fittings, and valve) were purchased from IDEX and washed sequentially in anhydrous Acetone and IPA. They were then dried under dynamic vacuum for 2 h and purged with Ar. The parts were then stored in Glovebox ($O_2 < 0.1$ ppm, $H_2O < 0.1$ ppm) before use.

Once dried, the cell and the microfluidic parts were transferred to a dry room for tubing positioning and microfluidic port assembly (Figures S1,S3,S7). The PEEK capillary tubing (length ~5 cm, outer diameter 790 µm, inner diameter 250 µm) was placed as shown in Figure S1, and electrolyte was infiltrated via the capillary to wet and fill the pouch cell. We used 1.0 mL LP57 electrolyte (3:7 EC/EMC +1 M $LiPF_6$, SoulBrain certified < 20 ppm $H_2O$, stored in Glovebox Ar atmosphere with $O_2 < 0.1$, $H_2O < 0.1$ ppm). Cells were gently massaged, and the Microfluidic port was closed prior to Pouch cell vacuum sealing (MTI compact vacuum sealer, -70 kPa, 150°C, 10s sealing time). Next, cells were immediately connected to a 1.5 V potentiostat for 12 h to avoid copper current collector dissolution and favor electrolyte diffusion in the separator.

### 5.2 | Electrochemical Cell Formation and Cycling

After cell resting, the cells were connected to a potentiostat for charge/discharge protocol with a designed upper-cut voltage (either 4.0 V or 4.3 V) and a 2.5 V lower cut voltage for two formation cycles performed at C/10 C-rate (Figure S1e), based on the nominal capacity of 200 mAh specified by the manufacturer. After the formation cycle and a further 48-h rest period, the cells were cycled at C/3 (66 mAh) for the desired ageing cycles. All the galvanostatic charge/discharge tests were performed in a temperature-controlled atmosphere (25°C formation and 40°C cycling). Cells were cycled at 40°C to accelerate ageing processes while remaining within the commonly used temperature range for degradation studies of Ni-rich NMC pouch cells [44].

### 5.3 | Electrolyte Extraction

Pouch cell cycling was stopped at the designed charge/discharge cycle (79, 210, 400) and allowed to rest vertically for 48 h to equalise any possible difference in concentration between the liquid electrolyte trapped in the separator and the excess electrolyte, which will be sampled. Prior to Raman analysis, cells were placed in a crystallizer and warmed to 40°C for 2 h on a hot plate, then transferred to the optical table and plugged to the hollow-core sensor, which was prefilled with pristine electrolyte. Approximately 3 mm of the tubing connected to the sensor was removed to clear the way from possible solidified EC electrolyte and secure the sampling. Once the optical setup was adjusted, we started the sampling procedure described in the supporting information (Figure S7a) and the Raman signal was monitored until obvious changes were detected and/or 40–60 µL of electrolyte volume was sampled using a Python automated pressure controller/flow meter (Fluigent). Flow rate and pressure were recorded during the sampling process (Figure S7,b).

The microsampling volume (40–60 µL per extraction point) was defined based on the electrolyte inventory and cell assembly protocol. During assembly, 3–4 mL of electrolyte was introduced under vacuum to ensure complete wetting of the separator and electrode stack; this volume primarily saturates the porous components and does not represent freely available excess electrolyte. An additional ~1 mL of excess electrolyte was included to

compensate for operando sampling. Each extraction event (≈40–60 µL) corresponds to ~1–2% of the total electrolyte volume, while the three sampling points (~200 µL total) represent ~20% of the excess electrolyte reservoir. Sampling, therefore, predominantly accesses the excess electrolyte region and does not significantly perturb electrolyte balance within the electrode stack.

### 5.4 | Electrolyte Sampling and Raman Acquisition

Spontaneous Raman measurements were acquired on a custom-built Python-automated Raman setup. Excitation and collection were performed through a 10 × 0.3 NA Olympus Plan Fluorite objective. Spectra were recorded by a Pixis 1024-element cooled CCD camera coupled to an Acton SP-2300i Spectrometer (Teledyne Princeton Instruments, USA). A grating with a period of 1200 grooves per mm was combined with a 190 µm entrance slit to obtain high-resolution scans over a 358 $cm^{-1}$ spectral window. Final spectral resolution is 2.4 $cm^{-1}$. A Python interface code performed automated scans and pressure controller. Aperture was selected to enable facet 0-th order imaging of the fibre facet and optical alignment of the laser pump into the sensor's hollow-core fibre. Raman spectra were baseline corrected using asymmetrically reweighted penalized least squares smoothing; spectra were subsequently scaled to the optical power of the laser pump during acquisition (typically ~130 mW at the sample at 785 nm) and normalized relative to the total spectral area to compare different datasets (see Figure S4). In the hollow-core waveguide configuration used here, small variations in refractive index and optical coupling can influence absolute Raman intensities; total-area normalization was therefore found to provide a more robust comparison than referencing individual solvent bands. Spectra were acquired with a 60 s integration time and averaged over three consecutive acquisitions. Laser power was monitored during measurements (Figure S4) and, after correction for optical losses at the dichroic, fluctuations remained below 5% over the acquisition period. Under these conditions, relative baseline noise levels were typically below ~1% of the signal intensity. For each voltage condition and cycling protocol, two independent pouch cells were tested (n = 2). Raman sampling and reinjection experiments were performed in duplicate to confirm reproducibility of the observed trends.

### 5.5 | Pouch Cells Rejuvenation by Electrolyte Refilling

LP57 pristine electrolyte was injected into the cycled cells at designated cycle numbers after interrupting the electrochemical cycling in a discharge state. Cells were transferred to a dry room (dew point -60°C), approximately 1 mm of the distal PEEK tubing was trimmed to ensure unobstructed electrolyte flow to the valve (see figure SI), to make sure that no residual material was impeding the flow of the electrolyte. Previously vacuum oven-dried (120°C, 30 mins) glass syringe and capillary tubing were used to infuse into the cells pristine LP57 electrolyte in the desired amount. The cells replenished with pristine LP57 electrolyte were then left resting for 96 h to allow the electrolyte to wet and equilibrate before restarting the electrochemical cycling.

### 5.6 | Hollow-core Fibre

The Nested Nodeless Antiresonant Fibre (NANF), N34C01B01, was obtained from the University of Southampton. Details of the characterization process can be found within previous work [32, 36, 49].

The guidance characteristics of this type of microstructured fibre can be explained using the anti-resonant reflecting optical waveguide (ARROW) model [50]. According to this model, light leakage occurs at resonant wavelengths, while at anti-resonant wavelengths, the cladding acts as a reflective barrier, enabling light propagation within the fibre. For a fibre filled with a typical electrolyte mixture (refractive index at 785 nm $n_1$ ~1.39) and glass cladding refractive index of $n_2 = 1.454$, and a capillary wall (strut) thickness of t = 590 ± 10 nm, the lowest-order (m = 1) resonance (loss wavelength) is $\lambda_R = (2t/m)\sqrt{n_2^2 - n_1^2}$ =503 nm, while the first (l = 0) anti-resonant wavelength is predicted as $\lambda_{AR} = 4t/(2l+1)\sqrt{n_2^2 - n_1^2}$ =1007 nm. This means that light guidance is expected in the desired Raman scattering spectral range of interest (797-931 nm or 200–2000 $cm^{-1}$, for a Raman pump at 785 nm, see Figure S3d). Indeed, the transmission efficiency of light through a 10–20 cm long electrolyte-filled fibre was observed to range between 30–40% (not shown). It is worth noting that the fibre's guiding behavior is relatively insensitive to variations in the electrolyte refractive index (see Supplementary Figure 3d).

### 5.7 | Microfluidic Pressure Cell

We minimised the compliance and dead volume of the fluidic connections to reduce the fluidic response time of the system during sample exchanges. The proximate end of the fibre is connected to a specially designed low-volume stainless-steel cell, covered by a sapphire optical access window (Edmund Optics), resulting in an internal volume of 230 nL. The geometry of the fibre embedded in the pouch cell is detailed in Figures S1 and S3. The microfluidic sampling line was assembled with Polyether ether ketone (PEEK) parts and Zero-Dead-Volume (ZDV) fittings (IDEX Health & Science, LLC, USA).

#### Acknowledgements

The authors thank Megan Groom for assistance in cycling measurements in Figure 3 and Figure S9. The Authors also thank Farheen Sayed for assistance in running the cycling experiments in Figure 3. This work is supported by the Faraday Institution under grant number FIRG024, the EPSRC [grants no: EP/P030181/1, UKRI1255, UKRI3173]. T.G.E. also acknowledges support from the Winton Program for the Physics of Sustainability. N.W. gratefully acknowledges support from a Royal Society University Research Fellowship.

#### Conflicts of Interest

During the writing and revision of this manuscript, Ermanno Miele was affiliated with Knowlitech Ltd. The company had no involvement in this work and does not commercialize the technology presented. The authors declare no conflicts of interest.

## Data Availability Statement

The data that support the findings of this study are available from the corresponding author upon reasonable request.

## References


1. C. P. Grey and J. M. Tarascon, "Sustainability and In Situ Monitoring in Battery Development," *Nature Materials* 16 (2017): 45–56, https://doi.org/10.1038/nmat4777.

2. J. Huang, S. T. Boles, and J.-M. Tarascon, "Sensing as the Key to Battery Lifetime and Sustainability," *Nature Sustainability* 5 (2022): 194–204, https://doi.org/10.1038/s41893-022-00859-y.

3. M. Kandhasamy, B. K. Duvaragan, S. Kamaraj, and G. Shanmugam, "An Overview on Classification of Energy Storage Systems" in *ACS Symposium Series* eds.S. S. Kumar, P. Sharma, and T. Kumar (American Chemical Society 2024): 1484 1–25.

4. N. Rogalev, A. Rogalev, V. Kindra, V. Naumov, and I. Maksimov, "Comparative Analysis of Energy Storage Methods for Energy Systems and Complexes," *Energies* 15 (2022): 9541.

5. S. Sabihuddin, A. Kiprakis, and M. Mueller, "A Numerical and Graphical Review of Energy Storage Technologies," *Energies* 8 (2014): 172–216.

6. F. A. Lopez, D. Lauinger, F. Vuille, and D. B. Müller, "On the Potential of Vehicle-to-grid and Second-life Batteries to Provide Energy and Material Security," *Nature Communications* 15 (2024): 4179, https://doi.org/10.1038/s41467-024-48554-0.

7. T. Brown, D. Schlachtberger, A. Kies, S. Schramm, and M. Greiner, "Synergies of Sector Coupling and Transmission Reinforcement in a Cost-optimized, Highly Renewable European Energy System," *Energy* 160 (2018): 720.

8. C. P. Grey and D. S. Hall, "Prospects for Lithium-ion Batteries and Beyond—a 2030 Vision," *Nature Communications* 11 (2020): 6279, https://doi.org/10.1038/s41467-020-19991-4.

9. H. Ruan, J. V. Barreras, T. Engstrom, Y. Merla, R. Millar, and B. Wu, "Lithium-ion battery lifetime extension: A review of derating methods," *Journal of Power Sources* 563 (2023): 232805, https://doi.org/10.1016/j.jpowsour.2023.232805.

10. S. Chen, G. Wu, H. Jiang, et al., "External Li Supply Reshapes Li Deficiency and Lifetime Limit of Batteries," *Nature* 638 (2025): 676–683, https://doi.org/10.1038/s41586-024-08465-y.

11. S. Goriparti, E. Miele, F. De Angelis, E. Di Fabrizio, R. P. Zaccaria, and C. Capiglia, "Review on Recent Progress of Nanostructured Anode Materials for Li-ion Batteries," *Journal of Power Sources* 257 (2014): 421–443, https://doi.org/10.1016/j.jpowsour.2013.11.103.

12. U. Gulzar, S. Goriparti, E. Miele, et al., "Next-generation Textiles: From Embedded Supercapacitors to Lithium Ion Batteries," *Journal of Materials Chemistry A* 4 (2016): 16771–16800, https://doi.org/10.1039/C6TA06437J.

13. W. Xue, M. Huang, Y. Li, et al., "Ultra-high-voltage Ni-rich Layered Cathodes in Practical Li Metal Batteries Enabled by a Sulfonamide-based Electrolyte," *Nature Energy* 6 (2021): 495–505, https://doi.org/10.1038/s41560-021-00792-y.

14. T. Yang, D. Luo, A. Yu, and Z. Chen, "Enabling Future Closed-Loop Recycling of Spent Lithium-Ion Batteries: Direct Cathode Regeneration," *Advanced Materials* 35 (2023): 2203218, https://doi.org/10.1002/adma.202203218.

15. W. M. Dose, I. Temprano, J. P. Allen, et al., "Electrolyte Reactivity at the Charged Ni-Rich Cathode Interface and Degradation in Li-Ion Batteries," *ACS Applied Materials & Interfaces* 14 (2022): 13206–13222, https://doi.org/10.1021/acsami.1c22812.

16. C. Xu, Q. Dai, L. Gaines, M. Hu, A. Tukker, and B. Steubing, "Future Material Demand for Automotive Lithium-based Batteries," *Communications Materials* 1 (2020): 99, https://doi.org/10.1038/s43246-020-00095-x.

17. A. Manthiram, "A Reflection on Lithium-ion Battery Cathode Chemistry," *Nature Communications* 11 (2020): 1550, https://doi.org/10.1038/s41467-020-15355-0.

18. Z. Li, H. Rao, R. Atwi, et al., "Non-polar Ether-based Electrolyte Solutions for Stable High-Voltage Non-Aqueous Lithium Metal Batteries," *Nature Communications* 14 (2023): 868, https://doi.org/10.1038/s41467-023-36647-1.

19. C.-Y. Li, Y. Yu, C. Wang, et al., "Surface Changes of LiNi x Mn y $Co_{1-x-y}O_2$ in Li-Ion Batteries Using in Situ Surface-Enhanced Raman Spectroscopy," *The Journal of Physical Chemistry C* 124 (2020): 4024–4031, https://doi.org/10.1021/acs.jpcc.9b11677.

20. C. Xu, K. Märker, J. Lee, et al., "Bulk Fatigue Induced by Surface Reconstruction in Layered Ni-rich Cathodes for Li-ion Batteries," *Nature Materials* 20 (2021): 84–92, https://doi.org/10.1038/s41563-020-0767-8.

21. T. Liu, J. Liu, L. Li, et al., "Origin of Structural Degradation in Li-rich Layered Oxide Cathode," *Nature* 606 (2022): 305–312, https://doi.org/10.1038/s41586-022-04689-y.

22. W. M. Dose, C. Xu, C. P. Grey, and M. F. L. De Volder, "Effect of Anode Slippage on Cathode Cutoff Potential and Degradation Mechanisms in Ni-Rich Li-Ion Batteries," *Cell Reports Physical Science* 1 (2020): 100253, https://doi.org/10.1016/j.xcrp.2020.100253.

23. W. M. Dose, W. Li, I. Temprano, et al., "Onset Potential for Electrolyte Oxidation and Ni-Rich Cathode Degradation in Lithium-Ion Batteries," *ACS Energy Letters* 7 (2022): 3524–3530, https://doi.org/10.1021/acsenergylett.2c01722.

24. D. M. C. Ould, S. Menkin, H. E. Smith, et al., "Sodium Borates: Expanding the Electrolyte Selection for Sodium-Ion Batteries," *Angewandte Chemie* 134 (2022): 202202133, https://doi.org/10.1002/ange.202202133.

25. S. Goriparti, E. Miele, M. Prato, et al., "Direct Synthesis of Carbon-Doped TiO 2 –Bronze Nanowires as Anode Materials for High Performance Lithium-Ion Batteries," *ACS Applied Materials & Interfaces* 7 (2015): 25139–25146, https://doi.org/10.1021/acsami.5b06426.

26. J. A. Gilbert, I. A. Shkrob, and D. P. Abraham, "Transition Metal Dissolution, Ion Migration, Electrocatalytic Reduction and Capacity Loss in Lithium-Ion Full Cells," *Journal of The Electrochemical Society* 164 (2017): A389–A399, https://doi.org/10.1149/2.1111702jes.

27. Z. Ruff, C. Xu, and C. P. Grey, "Transition Metal Dissolution and Degradation in NMC811-Graphite Electrochemical Cells," *Journal of The Electrochemical Society* 168 (2021): 060518, https://doi.org/10.1149/1945-7111/ac0359.

28. H. Adenusi, G. A. Chass, S. Passerini, K. V. Tian, and G. Chen, "Lithium Batteries and the Solid Electrolyte Interphase (SEI)—Progress and Outlook," *Advanced Energy Materials* 13 (2023): 2203307, https://doi.org/10.1002/aenm.202203307.

29. S. K. Heiskanen, J. Kim, and B. L. Lucht, "Generation and Evolution of the Solid Electrolyte Interphase of Lithium-Ion Batteries," *Joule* 3 (2019): 2322–2333, https://doi.org/10.1016/j.joule.2019.08.018.

30. C. Gervillié-Mouravieff, C. Boussard-Plédel, J. Huang, et al., "Unlocking Cell Chemistry Evolution with Operando Fibre Optic Infrared Spectroscopy in Commercial Na(Li)-ion Batteries," *Nature Energy* 7 (2022): 1157–1169, https://doi.org/10.1038/s41560-022-01141-3.

31. E. Miele, W. M. Dose, I. Manyakin, et al., "Hollow-core Optical Fibre Sensors for Operando Raman Spectroscopy Investigation of Li-ion Battery Liquid Electrolytes," *Nature Communications* 13 (2022): 1651, https://doi.org/10.1038/s41467-022-29330-4.

32. M. J. Groom, E. Miele, J. Pinnell, et al., "Microlens Hollow-Core Fiber Probes for Operando Raman Spectroscopy," *ACS Photonics* 11 (2024): 3167–3177.

33. I. Temprano, J. Carrasco, M. Bugnet, et al., "Advanced Methods for Characterizing Battery Interfaces: Towards a Comprehensive Understanding of Interfacial Evolution in Modern Batteries," *Energy Storage Materials* 73 (2024): 103794, https://doi.org/10.1016/j.ensm.2024.103794.

34. D. Castelvecchi, "Electric Cars and Batteries: How Will the World Produce Enough?," *Nature* 596 (2021): 336–339, https://doi.org/10.1038/d41586-021-02222-1.

35. R. Ma, S. Tao, X. Sun, et al., "Pathway Decisions for Reuse and Recycling of Retired Lithium-ion Batteries Considering Economic and Environmental Functions," *Nature Communications* 15 (2024): 7641, https://doi.org/10.1038/s41467-024-52030-0.

36. H. Sakr, Y. Chen, G. T. Jasion, et al., "Hollow Core Optical Fibres With Comparable Attenuation to Silica Fibres Between 600 and 1100 nm," *Nature Communications* 11 (2020): 6030, https://doi.org/10.1038/s41467-020-19910-7.

37. C. Xu, A. J. Merryweather, S. S. Pandurangi, et al., "Operando Visualization of Kinetically Induced Lithium Heterogeneities in Single-particle Layered Ni-rich Cathodes," *Joule* 6 (2022): 2535.

38. I. A. Moiseev, A. A. Savina, A. D. Pavlova, et al., "Single Crystal Ni-rich NMC Cathode Materials For Lithium-Ion Batteries With Ultra-High Volumetric Energy Density," *Energy Adv* 1 (2022): 677.

39. G. J. Páez Fajardo, E. Fiamegkou, J. A. Gott, et al., "Synergistic Degradation Mechanism in Single Crystal Ni-Rich NMC//Graphite Cells," *ACS Energy Letters* 8 (2023): 5025–5031, https://doi.org/10.1021/acsenergylett.3c01596.

40. A. Wang, S. Kadam, H. Li, S. Shi, and Y. Qi, "Review on Modeling of the Anode Solid Electrolyte Interphase (SEI) for Lithium-ion Batteries," *npj Computational Materials* 4 (2018): 15, https://doi.org/10.1038/s41524-018-0064-0.

41. Y. Zhang, Y. Katayama, R. Tatara, et al., "Revealing Electrolyte Oxidation via carbonate Dehydrogenation on Ni-based Oxides in Li-ion Batteries by In Situ Fourier Transform Infrared Spectroscopy," *Energy & Environmental Science* 13 (2020): 183–199, https://doi.org/10.1039/C9EE02543J.

42. B. L. D. Rinkel, D. S. Hall, I. Temprano, and C. P. Grey, "Electrolyte Oxidation Pathways in Lithium-Ion Batteries," *Journal of the American Chemical Society* 142 (2020): 15058–15074, https://doi.org/10.1021/jacs.0c06363.

43. L. Britala, M. Marinaro, and G. Kucinskis, "A Review of the Degradation Mechanisms of NCM Cathodes and Corresponding Mitigation Strategies," *Journal of Energy Storage* 73 (2023): 108875, https://doi.org/10.1016/j.est.2023.108875.

44. G. J. P. Fajardo, M. Belekoukia, S. Bolloju, et al., "Understanding Improved Capacity Retention at 43 V in Modified Single Crystal Ni-rich NMC//Graphite Pouch Cells at Elevated Temperature," *RSC Applied Interfaces* 1 (2024): 133–146.

45. E. Sarasketa-Zabala, F. Aguesse, I. Villarreal, L. M. Rodriguez-Martinez, C. M. López, and P. Kubiak, "Understanding Lithium Inventory Loss and Sudden Performance Fade in Cylindrical Cells During Cycling With Deep-Discharge Steps," *The Journal of Physical Chemistry C* 119 (2015): 896–906.

46. Y. Yu, P. Karayaylali, Y. Katayama, et al., "Coupled LiPF6 Decomposition and Carbonate Dehydrogenation Enhanced by Highly Covalent Metal Oxides in High-Energy Li-Ion Batteries," *The Journal of Physical Chemistry C* 122 (2018): 27368–27382, https://doi.org/10.1021/acs.jpcc.8b07848.

47. N. Kirkaldy, M. A. Samieian, G. J. Offer, M. Marinescu, and Y. Patel, "Lithium-Ion Battery Degradation: Measuring Rapid Loss of Active Silicon in Silicon–Graphite Composite Electrodes," *ACS Applied Energy Materials* 5 (2022): 13367–13376, https://doi.org/10.1021/acsaem.2c02047.

48. P. M. Attia, A. Bills, F. Brosa Planella, et al., "Review—"Knees" in Lithium-Ion Battery Aging Trajectories," *Journal of The Electrochemical Society* 169 (2022): 060517.

49. T. D. Bradley, G. T. Jasion, J. R. Hayes, et al., "Record low-loss 1.3 dB/km Data Transmitting Antiresonant Hollow Core Fibre," 2018 European Conference on Optical Communication n/a (2019): 1–3, https://doi.org/10.1109/ECOC.2018.8535324.

50. N. M. Litchinitser, A. K. Abeeluck, C. Headley, and B. J. Eggleton, "Antiresonant Reflecting Photonic Crystal Optical Waveguides," *Optics Letters* 27, 18 (2002): 1592, https://doi.org/10.1364/OL.27.001592.

## Supporting Information

Additional supporting information can be found online in the Supporting Information section.

**Supporting File**: admt70948-sup-0001-SuppMat.docx.